https://doi.org/10.20965/jdr.2017.p0967

Paper:

Very Short Time Range Forecasting Using CReSS-3DVAR for a Meso-γ-Scale, Localized, Extremely Heavy Rainfall Event: Comparison with an Extrapolation-Based Nowcast

Ryohei Kato†, Shingo Shimizu, Ken-ichi Shimose, and Koyuru Iwanami

Storm, Flood and Landslide Research Division, National Research Institute for Earth Science and Disaster Resilience (NIED)
3-1 Tennodai, Tsukuba, Ibaraki 305-0006, Japan
†Corresponding author, E-mail: katon@gfd-dennou.org
[Received April 3, 2017; accepted September 19, 2017]

The forecast accuracy of a numerical weather prediction (NWP) model for a very short time range (≤1 h) for a meso-γ-scale (2–20 km) extremely heavy rainfall (MγExHR) event that caused flooding at the Shibuya railway station in Tokyo, Japan on 24 July 2015 was compared with that of an extrapolation-based nowcast (EXT). The NWP model used CReSS with 0.7 km horizontal grid spacing, and storm-scale data from dense observation networks (radars, lidars, and microwave radiometers) were assimilated using CReSS-3DVAR. The forecast accuracy of the heavy rainfall area (≥20 mm h^{-1}), as a function of forecast time (FT), was investigated for the NWP model and EXT predictions using the fractions skill score (FSS) for various spatial scales of displacement error (L). These predictions were started 30 minutes before the onset of extremely heavy rainfall at Shibuya station. The FSS for L=1 km, i.e., grid-scale verification, showed NWP accuracy was lower than that of EXT before FT=40 min; however, NWP accuracy surpassed that of EXT from FT=45 to 60 min. This suggests the possibility of seamless, high-accuracy forecasts of heavy rainfall (≥20 mm h^{-1}) associated with MγExHR events within a very short time range (≤1 h) by blending EXT and NWP outputs. The factors behind the fact that the NWP model predicted heavy rainfall area within the very short time range of ≤1 h more correctly than did EXT are also discussed. To enable this discussion of the factors, additional sensitivity experiments with a different assimilation method of radar reflectivity were performed. It was found that a moisture adjustment above the lifting condensation level using radar reflectivity was critical to the forecasting of heavy rainfall near Shibuya station after 25 min.

Keywords: meso-γ-scale extreme heavy rainfall, numerical weather prediction, extrapolation-based nowcast, blending, predictability

1. Introduction

Meso-γ-scale (2–20 km) extremely heavy rainfall (MγExHR) events can cause urban flash flooding with accompanying damage and potential loss of life, e.g., [1, 2]. Therefore, the development and verification of an appropriate forecasting methodology for MγExHRs is very important.

There are two principal approaches to the forecasting of rainfall on very short temporal scales, termed "nowcasting." The first approach is called extrapolation-based nowcast (EXT), in which a precipitation variable such as rainfall rate is extrapolated temporally using radar data, e.g., [3, 4]. However, a simple extrapolation-based nowcast cannot incorporate storm evolution: initiation, growth, and dissipation. Therefore, EXT accuracy is generally highest in the very short term, and it decreases rapidly with time. The second approach to forecasting rainfall uses numerical weather prediction (NWP) models, e.g. [5]. In NWP models, time is needed to create precipitation if the models, in their initial conditions, do not include precipitation at the start of the forecast. The assimilation of radar reflectivity at the start of a forecast can reduce the time needed to create precipitation. However, it is difficult to embed thermodynamically-balanced, small-scale convective features with precipitation in the model initial conditions and then to correctly evolve these features. The time needed to create such balanced convective features with precipitation is called the "spin-up time," and the existence of the spin-up time inherent in NWP models is referred to as the "spin-up problem" (e.g., [6]). Because of the spin-up problem, NWP model accuracy is generally low in the very short term. Over longer periods, the forecast accuracy of NWP models tends to be better than that of EXTs, primarily because NWP models are able to simulate storm lifecycles through the consideration of related atmospheric processes.

Kato et al. (2017) [7] examined the predictability, or the forecast accuracy as a function of forecast time, of 23 selected MγExHR events (1-h accumulation rainfall ≥50 mm) that occurred during the warm season of 2014 in Japan, using High-Resolution Precipitation Nowcasts (HRPNs) [8, 9] provided by the Japan Meteorological Agency (JMA). Although the HRPNs incorporate prediction algorithms for the initiation, growth, and dissipation of heavy rainfall areas, the HRPNs are based on extrapolation, i.e., EXTs, and differ from NWP, which

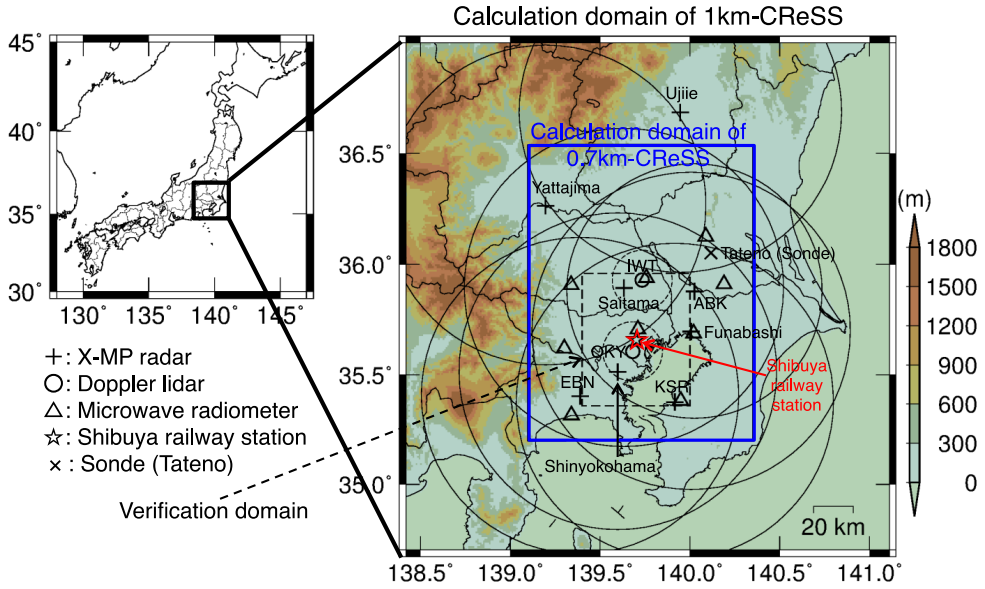

Fig. 1. Calculation domains of 1km-CReSS and 0.7km-CReSS experiments as well as locations of observation stations. Circles indicate the observational ranges of the radars (solid circles) and lidars (dashed circles). The different colors indicate topographic elevations.

time-integrates hydrodynamic and thermodynamic equations with cloud physics. Kato et al. (2017) [7] showed that the predictability limit for areas of heavy rainfall ($\geq$20 mm h^{-1}) was $\sim$30 min if a displacement error (L) of $\sim$10 km is tolerated. Strictly speaking, L indicates neighborhood length in calculating the fractions skill score (FSS) [10]. This suggests that NWP models with acceptable accuracy beyond $\sim$30 min for areas of heavy rainfall ($\geq$20 mm h^{-1}, L: $\sim$10 km) are necessary for useful forecasts to be provided beyond this time limit. If such an NWP model exists, it should be possible to provide useful forecasts of the heavy rainfall areas associated with MγExHR events by seamlessly blending the HRPN and NWP outputs.

Most blending methods are intended to improve forecast accuracy for large-scale ($\geq$meso-β-scale) precipitation events over a time range of more than several hours (e.g., [11]), whereas the applicability of blending methods to MγExHR events on very short time scales ($\leq$1 h) has rarely been examined. This is partly because of the lower forecast accuracy of NWP models over a very short time range due to spin-up problems. However, these have recently been reduced by storm-scale data assimilation in high-resolution, rapid-update-cycle NWP models [5].

There have been earlier studies of MγExHR events using NWP models with storm-scale data assimilation (e.g., [12, 13]); however, they did not compare the accuracies of NWP models and EXTs. Therefore, it is necessary to investigate first whether NWP accuracy for MγExHRs can outperform that of EXTs before examining the applicability of a blending method for MγExHRs.

In this study, we investigated and compared the forecast accuracies of an NWP model and those of EXT over a very short time range ($\leq$1 h) for an MγExHR event that caused flooding at the Shibuya railway station in Tokyo, Japan on 24 July 2015. For the EXT, we used HRPNs provided by the JMA. For the NWP model, a high-resolution (0.7 km) cloud-resolving storm simulator (CReSS) [14, 15] was used with a three-dimensional variational (3DVAR) data assimilation system called CReSS-3DVAR. For the CReSS-3DVAR, unique storm-scale observational data obtained from dense networks of radars, lidars, and microwave radiometers (MWRs), developed in the Tokyo metropolitan area by the National Research Institute for Earth Science and Disaster Resilience (NIED), were assimilated. The unique aspect of this study was the comparison of the forecast accuracies of the NWP model and EXT within a very short time range ($\leq$1 h) for an MγExHR event.

The remainder of this paper is organized as follows. In section 2, the observational data and CReSS-3DVAR system are explained. In section 3, a brief introduction of the HRPN data is presented. In section 4, the verification methods that use FSS are explained. The results are presented in section 5 and discussed in section 6. Finally, a summary of the study and thoughts regarding future work are given in section 7.

2. Observations and Assimilation System of CReSS-3DVAR

2.1. Observations

2.1.1. Radar

For the assimilation of radar reflectivity, five X-band multiparameter (X-MP) Doppler radars [16] operated by Japan's Ministry of Land, Infrastructure, Transport, and Tourism were used (Shinyokohama, Funabashi, Saitama, Yattajima, and Ujiie; **Fig. 1**). The observation range of the radars was 80 km. The radial and azimuthal sam-

pling intervals of the radars were 150 m and 1.2°, respectively. Quality control of the radar reflectivity data was conducted to eliminate noise, ground clutter, and non-meteorological echoes with the help of polarimetric parameters [16]. The attenuation of reflectivity was corrected using specific attenuation calculated from a specific differential phase [16]. The radars were operated in a volume-scan mode with 12 elevation angles (0.5° –20.0°) every 5 min.

For the assimilation of radial velocity, eight X-MP Doppler radars were used, including the five mentioned above. The other three radars were research radars: two that belonged to NIED, located at Ebina (EBN) and Kisarazu (KSR), and one that belonged to the Central Research Institute of the Electric Power Industry, located at Abiko (ABK). The beam widths of the EBN and KSR radars were 1.3° and 1.0°, respectively, and the observational range of these radars was 80 km. The beam width and observational range of the ABK were 1.2° and 64 km, respectively. The radial sampling interval of the EBN, KSR, and ABK radars was 150 m. The EBN and KSR radars were operated in a volume-scan mode with 10 elevation angles (0.7°–6.9°) every 5 min. The ABK radar was operated in a volume-scan mode with 14 elevation angles (0.6°–24.4°) every 5 min.

For both the reflectivity and the radial velocity data, 5 minutes of observational data before the starting time of the NWP forecast (13:55–14:00 JST) were assimilated. JST stands for Japan Standard Time (JST = UTC + 9 h).

2.1.2. Lidar

The two Doppler lidars used in this study were developed by the Mitsubishi Electric Corporation and NIED, and they were located at Okayama (OKY) and Iwatsuki (IWT) (**Fig. 1**). These lidars observed radial velocity using an eye-safe laser with a wavelength of 1.55 μm. The laser of this wavelength is strongly backscattered by aerosols. The pulse width was 500 ns and the pulse repetition frequency was 4000 Hz. The range and azimuthal sampling intervals were 150 m and 1°, respectively. The observational range typical during summer was approximately 15 km, depending on atmospheric conditions. In this study, 10 minutes of radial velocity data before the starting time of the NWP forecast (13:50–14:00 JST) were assimilated. The data included one scan of plan position indicator (PPI) from the IWT lidar (elevation angle = 6.9°, rotation speed RS = 240 deg min^{-1}, sampling number: number of Doppler spectra averaged for Doppler velocity N = 1000), and two scans of PPI from the OKY lidar (elevation angle = 1.9°, RS = 240 and 60 deg min^{-1}, N = 1000 and 4000).

2.1.3. Microwave Radiometer (MWR)

The MWR network with 10 MWRs was developed in 2014 by NIED in the Tokyo metropolitan area, and continuous observations using the MWR network commenced in April 2015. The MWRs used in this study were Humidity And Temperature PROfilers (HATPRO) models manufactured by Radiometer Physics Gmbh (Germany). Using the MWRs, precipitable water vapor (PWV) was retrieved based on statistical analysis with a neural networking method [17] using a training set of radiosonde upper sounding data from the past 30 years (09:00 and 21:00 JST), observed at Tateno (**Fig. 1**). Seven channels of brightness temperature in the water vapor absorption band (22.24–31.4 GHz) and seven channels of brightness temperature in the oxygen absorption band (51.0–58.0 GHz) were used. In this study, 9 of the 10 MWRs which were normally working were used to retrieve the horizontal distribution of PWV, and the PWV was assimilated using the 3DVAR. In this study, 5 minutes of averaged observational data before the starting time of the NWP forecast (13:55–14:00 JST) were assimilated.

2.2. CReSS

Forecast experiments were conducted using CReSS [14, 15]. The basic equations of CReSS are composed of the Navier-Stokes equations with a map factor, the continuity equation, the equation of thermodynamics, and conservation equations related to microphysics. The vertical momentum equation is non-hydrostatic, and the continuity equation is expressed in a quasicompressible form. In the microphysics of CReSS, six species, namely, water vapor, cloud water, rainwater, cloud ice, snow, and graupel, are considered. In this study, a two-moment bulk cold-rain scheme was used [18], and the mixing ratio of the six species and number concentrations of ice, snow, and graupel were predicted. For the turbulence scheme, a 1.5-order closure with a turbulent kinematic energy prediction based on the method of [19, 20] was used. Surface fluxes of momentum and energy and the surface radiation process [21–23] were included.

2.3. Basic CReSS-3DVAR Schemes

The 3DVAR system is based largely on [24, 25] but modified appropriately for convective-scale data assimilation. The standard cost function of 3DVAR can be written as follows:

$$\begin{aligned} J(\mathbf{x}) &= \frac{1}{2}(\mathbf{x}-\mathbf{x}^b)^T\mathbf{B}^{-1}(\mathbf{x}-\mathbf{x}^b) \\ &+ \frac{1}{2}[H(\mathbf{x})-\mathbf{y}^o]^T\mathbf{R}^{-1}[H(\mathbf{x})-\mathbf{y}^o]+J_c(\mathbf{x}), \end{aligned} \quad (1)$$

where the first term on the right-hand side $J_b(\mathbf{x})$ measures the departure of the analysis vector $\mathbf{x}$ from the background $\mathbf{x}^b$, weighted by the inverse of the background error covariance matrix $\mathbf{B}$. In the current CReSS-3DVAR system, the analysis vector $\mathbf{x}$ contains the three wind components (u, v, and w) and pseudo relative humidity (q_u; [26]). Hydrometeors are not analyzed variationally. Cross correlations between different types of variable are not included in $\mathbf{B}$, as is the case in most convective-storm-scale assimilation systems [27, 28]. The assumption of the lack of correlation between different types of variable is partly supported by the very small value of the background cross

correlation of forecast errors between u and v for a high horizontal resolution (2 km) and a short time range (4–5 h) forecast [27]. The second observation term $J_o(\mathbf{x})$ measures the departure of the analysis from the observation vector $\mathbf{y}^o$. The analysis is projected to the observation space by the forward observation operator H, and the observation term is weighted by the inverse of the observation error covariance matrix $\mathbf{R}$, which includes both instrument and representativeness errors. For simplification, the observation errors are assumed to be uncorrelated; hence, $\mathbf{R}$ is a diagonal matrix. Term $J_c(\mathbf{x})$ in Eq. (1) represents dynamic or equation constraints, which were set to zero in this study. The standard cost function $J(\mathbf{x})$ is changed into incremental form, and the square root of $\mathbf{B}$ is used [29, 30] to precondition the minimization problem effectively. The transformed cost function is minimized through a limited memory, quasi-Newton method (L-BFGS method) [31].

2.3.1. Radial Velocity from Radars and Lidars

For J_o in Eq. (1), the radial velocity obtained from the radars and lidars is a part of the observation vector $\mathbf{y}^o$. In the radar forward observation operator $H(\mathbf{x})$, the analysis (u, v, and w in $\mathbf{x}$) is a trilinear interpolation from model grid points to radar observation locations. The radial velocity is calculated from the interpolated wind vectors, with the effects of both Earth's curvature and refraction (downward bending) of the radar beam due to atmospheric stratification accounted for [32]. We assume $\mathbf{R}$ is diagonal with constant diagonal elements given by the standard deviations of the errors for the radial velocity of 1 m s^{-1} for both radars and lidars, i.e., the same values as those used in [12]). For radial velocity observations from the radars, low-elevation-angle ($\leq 10^\circ$) radial velocity was adjusted to remove the effect of the fall velocity of precipitation by using an empirical relationship between the reflectivity factor and the raindrop terminal fall velocity ([33], Eq. (2) in [34]). Since this relationship is empirical, some error in the estimation of the terminal fall velocity is included, and this error could be larger at higher angles of elevation. Thus, high-elevation-angle observations ($>10^\circ$) were neglected. For quality control, lidar radial velocity data with a signal-to-noise ratio of <12 were neglected for the assimilation. Further quality control for both radar and lidar data was conducted by removing spurious observational data with radial velocities that had differences from those of the first guess of the background of >40 m s^{-1}.

For J_b in Eq. (1), both horizontal and vertical components of $\mathbf{B}$ for u, v, and w were modeled by a spatial recursive filter (RF) [35–37]. For the RF, the horizontal correlation scale of u and v was set to 5 km, while that of w was set to 2 km. The vertical correlation scale of u and v was set to 2 km, while that of w was set to 1 km. These scales were estimated using the National Meteorological Center (NMC) method [38]. In the NMC method, 1-h forecast errors of CReSS that have a horizontal resolution of 1 km and 50 vertical levels are calculated for all grids, regardless of the occurrence of precipitation, from the differences of the 2-h and 3-h forecasts every 1 h during the summer season (August 2009–2011). Because the forecast errors calculated from the NMC method were climatological value, they were probably underestimated for severe convective events. Thus, the standard deviations of the background errors for u, v, and w were taken as 10 m s^{-1}, which were more than twice those calculated using the NMC method.

Note that w was included as a control variable in the CReSS-3DVAR, but we finally set the increment of w to zero as an initial condition of the CReSS integration. That is to say, vertical velocity at the start of the CReSS calculation was not modified by the assimilation of radial velocities. This procedure was partly supported by the fact that the assimilation system used radial velocities of low elevation angle ($\leq 10^\circ$) where the horizontal component of radial velocity was dominant. To introduce an appropriate vertical velocity field as an initial condition is a challenging task [39–41], and future works related to this will be described in section 6.

2.3.2. Precipitable Water Vapor Retrieved from the MWRs

For J_o in Eq. (1), the PWV obtained from the MWRs is a part of the observation vector $\mathbf{y}^o$. As PWV data represent the vertically integrated amount of water vapor from the altitude of the MWR receiver to the top of the atmosphere, the forward observation operator $H(\mathbf{x})$ of the MWR PWV is approximated as follows:

$$PWV_{model} = \sum_{k=model\_bottom}^{k=model\_top} q_{vk}\rho_k\Delta z_k \quad . \quad . \quad . \quad . \quad . \quad (2)$$

where q_v is the mixing ratio of water vapor, ρ is air density, and Δz_k is the thickness of the k-th vertical layer. These variables were bilinearly interpolated from model grid points to the MWR locations before the vertical integration. We assumed $\mathbf{R}$ was diagonal, with constant diagonal elements given by the standard deviations of the errors for PWV σ_{PWV} of 1.5 mm. Quality control was performed by rejecting data with $|\text{O-B}|>10$ mm, where O indicates the observation and B indicates the background.

For J_b in Eq. (1), the pseudo relative humidity [26] was chosen:

$$q_u = \frac{q_v}{q_{vs}^b} \quad . \quad . \quad . \quad . \quad . \quad . \quad . \quad . \quad . \quad . \quad . \quad . \quad . \quad . \quad . \quad . \quad . \quad (3)$$

where q_{vs}^b is the saturation mixing ratio of water vapor given by the background. The vertical component of $\mathbf{B}$ for q_u was diagonalized by empirical orthogonal functions (EOFs), using the NMC method explained above. The horizontal component of $\mathbf{B}$ for q_u was modeled by the RF with horizontal correlation scales (11 km for the 1st mode and <4 km for modes larger than the 2nd mode) estimated by each of the vertical modes of the EOFs. The standard deviation of the background error for q_u was 4.0% (3.7%) for the 1st (2nd) mode. The explained variance ratio was 25% (21%) for the 1st (2nd) mode.

2.4. Assimilation of Radar Reflectivity

Assimilation of radar reflectivity was performed outside the framework of the 3DVAR. With reflectivity data observed by the radars used, (a) the model first guess of the 3D field of precipitation (mixing ratio of rainwater q_r, snow q_s, and graupel q_g) and (b) the model first guess of the 3D field of relative humidity was modified. Approach (a) is similar to that of "cloud analysis" (e.g., [42]) in that the precipitation field is introduced in the first guess, but approach (a) differs in that the adjustment of cloud or temperature is not implemented. The idea behind approach (b) related to modifying humidity is similar to that of the "1D+3DVAR" method [43, 44]. In the "1D+3DVAR" method, (1D) vertical profiles of relative humidity are retrieved from observed vertical profiles of reflectivity through a Bayesian inversion method, which is followed by the implementation of the 3DVAR system. Approach (b) does not include such a Bayesian inversion method; instead, it modifies the 3D field of relative humidity using precipitation or no-precipitation information from the model and the observations. The method of radar reflectivity assimilation is explained in more detail below.

To perform the reflectivity assimilation, we first interpolated radar reflectivity from radar observation points to a model grid. We did not select an interpolation method using the radius of influence, e.g., Cressman interpolation, but we instead selected the RF for the interpolation because the processing speed of the RF is much faster than that of Cressman interpolation. The faster processing speed of RF is necessary for real-time forecasts with rapid updates (every ∼10 min) to be performed. The interpolation method using the RF is as follows. The PPI reflectivity data from those radars with values of ≥15 dBZ were remapped to the analysis grid, resulting in the remapped reflectivity value Z_{remap}. In the remapping procedure, observed reflectivity values in radar polar coordinates were simply substituted for the closest analysis Cartesian grid point and averaged with a weight of the distance from the radar grid point to the analysis grid if more than two values were substituted in the analysis grid. Then, to obtain a continuous reflectivity profile, especially in the vertical direction, the Z_{remap} was smoothed using the RF (six passes, i.e., six applications of a single RF) with the horizontal (vertical) correlation scale of 1.5 km (1.0 km), resulting in the smoothed reflectivity value Z_{smooth}. If Z_{smooth} was smaller than Z_{remap}, the value of Z_{remap} was used instead of Z_{smooth}. This replacement of reflectivity is important for the sharp distribution of the original reflectivity profile to be maintained. If this replacement were not performed, the distribution near the peak value of the original reflectivity would be flattened considerably by the RF, and this could result in underestimation of the forecast surface rainfall. Hereinafter, Z_{smooth} is referred to as Z for simplicity.

Secondly, the assessment of precipitation or no-precipitation was conducted in the following way. For the interpolated observed reflectivity, grid points were classified into clear or precipitation-filled categories, based on a 15-dBZ reflectivity threshold. This threshold was chosen because most non-hydrometeor targets, such as ground clutter, have reflectivity values <15 dBZ but often >0 dBZ. For the model, the grid points were classified into precipitation-filled categories by the same reflectivity threshold used for the observations: $10\log_{10}(Z(q_r) + Z(q_g) + Z(q_s)) \geq 15$ dBZ, where $Z(q_r)$, $Z(q_g)$, and $Z(q_s)$ indicate reflectivity retrieved from q_r, q_g, or, q_s by using Eqs. (4)–(6), explained below.

2.4.1. Adjustment of Precipitation Species from Radar Reflectivity

At grid points where precipitation was observed, the precipitation species (q_r, q_s, and q_g kg kg^{-1}) in the model were modified from the observed reflectivity factor (Z mm^6 m^{-3}). While at grid points where precipitation was not observed, the precipitation species (q_r, q_s, and q_g) in the model were set to zero. If the temperature was ≥0°C, q_r was calculated from Eq. (3) of [45] based on [46] as follows:

$$\begin{array}{lcl} q_r & = & 3.44506 \times 10^{-6} Z^{0.571} / \rho, \\ \text{from} \quad Z & = & 3.63 \times 10^9 (\rho q_r)^{1.75}, \end{array} \quad . \quad (4)$$

where ρ (kg m^{-3}) is atmospheric density. If the temperature was <0°C, precipitation species were categorized into graupel (q_g) and snow (q_s), depending on the value of the customary logarithmic scale (dBZ) of Z, i.e., Z_{db}. $= 10 \log_{10} Z$. If $Z_{db} \geq 45$(dBZ), the precipitation was categorized as graupel, and the reflectivity formulation of Eq. (15) in [47] was used, with

$$\begin{array}{lcl} q_g & = & 1.26 \times 10^{-6} Z^{0.571} / \rho \\ \Rightarrow \quad Z & = & 2.11036 \times 10^{10} (\rho q_g)^{1.75} \end{array} \quad . \quad . \quad (5)$$

If Z_{db} <45(dBZ), the precipitation was categorized as (dry) snow, and the reflectivity formulation of Eq. (4) of [45] was used, with

$$\begin{array}{lcl} q_s & = & 7.28042 \times 10^{-6} Z^{0.571} / \rho, \\ \text{from} \quad Z(q_s) & = & 9.80 \times 10^8 (\rho q_s)^{1.75} \end{array} \quad (6)$$

The hydrometeor classification method employed here was based on temperature and the reflectivity factor for horizontally polarized waves (i.e. single polarimetric information) for simplicity. It should be noted that the method leaves large ambiguities. For example, rain regions could exist below 0°C or graupel regions could exist below 45 dBZ. These ambiguities will likely decrease if dual polarimetric information is used for the hydrometeor classification. The use of the polarimetric information is left for future studies.

2.4.2. Adjustment of Moisture

Moisture was adjusted in a way similar to that in previous studies [39–41]. Through the moisture adjustment, the atmosphere of a grid was saturated. In other words, relative humidity was set to 100% if all of the following conditions were satisfied: (1) no precipitation was predicted in the model but precipitation was observed

(missed forecast), (2) the grid was above the lifting condensation level and (3) the grid was in convective regions of $Z_{db} \geq 35$ dBZ. To adjust relative humidity, the water vapor mixing ratio q_v was used in the following way. First, the increment of $q_v(dq_v)$ that was required to moisten the atmosphere was calculated. Second, the dq_v was smoothed using the RF (six passes) with the horizontal (vertical) correlation scale of 1.5 km (1.0 km). Lastly, dq_v was added to the first guess of q_v.

2.5. Design of the Assimilation Experiment

First, a large-domain forecast (2.691° × 2.295°, longitude × latitude) covering most of the Kanto Plain was conducted with 1-km horizontal grid spacing (1km-CReSS; **Fig. 1**) from 12:00–15:00 JST on 24 July 2015. The horizontal grid points were 300 ×256, and the time step of integration was set to 1 s. Initial and lateral boundary conditions of the 1km-CReSS were provided by the outputs of the JMA mesoscale model (JMA-MSM: [48]) initialized at 12:00 JST. Using the 1km-CReSS as the initial and lateral boundary conditions, a small-domain forecast (1.253°×1.157°) was conducted with 0.7-km horizontal grid spacing (0.7km-CReSS; **Fig. 1**) from 14:00–15:00 JST. The calculation domain covers the Tokyo metropolitan area, which has dense radar, lidar, and MWR observation networks. The horizontal grid points were 180 × 192, and the time step of integration was set to 0.5 s. The starting time of the 0.7km-CReSS forecast (14:00 JST) was 30 min before extremely heavy rainfall was observed at the Shibuya railway station.

The mutual settings for the 1km-CReSS and the 0.7km-CReSS forecasts are described in the following. The vertical grid contained 50 levels with variable grid intervals of 100 m near the surface and 350 m on average. The model top was set to 17.182 km. To set the initial sea surface temperature, we employed the Merged satellite and in situ data Global Daily Surface Temperatures (MGDSST) of the JMA, with a horizontal grid interval of 0.25°. Terrain and land use data in the simulation domain were determined using the GTOPO30 and Global Land Cover Characterization datasets (30-arcsecond elevation data produced by the U.S. Geological Survey's Earth Resources Observation System Data center). No cumulus parameterization was used.

The settings of the assimilation forecasts were as follows. As the control run, all types of available observational data were assimilated, i.e., the radial velocity (VR) from the radars and lidars, PWV from the MWRs, and radar reflectivity Z from the radars were assimilated for the 1km-CReSS and 0.7km-CReSS. In section 6, the assimilation impact of Z on the predicted surface rainfall rate is investigated briefly.

3. High-Resolution Precipitation Nowcasts

The HRPN data [8, 9], created by the JMA, were used as predictions for the EXTs. The data are provided to the public every 5 min, and they include both the analysis and the forecast of the rainfall rate at the surface. The forecast data include 5–60-min forecast times (FTs) with 5-min intervals. The HRPN data also include analysis at FT = 0 min, which was used as truth for verification. A horizontal grid spacing of $\Delta x = 250$ m was used for both the analysis (FT = 0 min) and the forecasts from FT = 5–30 min, and $\Delta x = 1$ km was used for the forecasts from FT = 35–60 min. A detailed description of the HRPN data can be found in [8, 9], and it is summarized in [7].

4. Verification Method

We verified the forecasts of the CReSS-0.7km and HRPNs at each forecast time by analysis of the HRPNs every 5 min during the verification period (14:00–15:00 JST) with a variable rainfall rate at the surface. As the HRPN data were provided with different resolutions (as outlined in section 3), the HRPN data of $\Delta x = 250$ m (FT = 0 to 30 min) were bilinearly interpolated onto $\Delta x =$ 1 km grids before verification, yielding $\Delta x = 1$ km data for FT = 0 to 60 min. The CReSS-3DVAR data were also bilinearly interpolated onto the $\Delta x = 1$ km grids.

Forecast accuracy was verified using FSS [10], which is often used for verifying precipitation (e.g. [7]). Using FSS, we can verify the closeness between an observed and forecast fractional occurrence of rainfall exceeding a given threshold for various values of L. To examine the sensitivity of L to the FSS, we used values of L = 1, 5, and 11 km, and in order to focus on heavy rainfall, we selected the threshold rainfall rate of 20 mm h^{-1} in calculating the FSS.

To focus on the heavy rainfall observed around Shibuya station, the verification area was set to 0.6°×0.6° (longitude × latitude) with its center over Shibuya station (**Fig. 1**). This verification area was within the dense observation area of radars, lidars, and MWRs, indicating the area benefits from assimilation with high probability.

5. Results

5.1. Summary of the MγExHR Event

The MγExHR event occurred on 24 July 2015. During the daytime hours that day, many localized meso-γ-scale heavy rainfall events occurred across the Kanto Plain under unstable atmospheric conditions. At around 12:00 JST, the convective storm that caused flooding at the Shibuya railway station developed to the west of the Tokyo metropolitan area, beyond the dense lidar and MWR observational networks. The convective storm propagated east-southeastward, and the extremely heavy rainfall that flooded the station occurred at around 14:30 JST. The 1-h accumulated rainfall analysis (P1h), created by the JMA using radars and rain gauges [11], recorded a maximum value of P1h ($P1h_{max}$) of 65 mm approximately 10 km west of the station at 15:00 JST. The horizontal scale of the heavy rainfall area L_h was 8.5 km, estimated from the enclosed areas of P1h ≥ 30 mm, indicating that

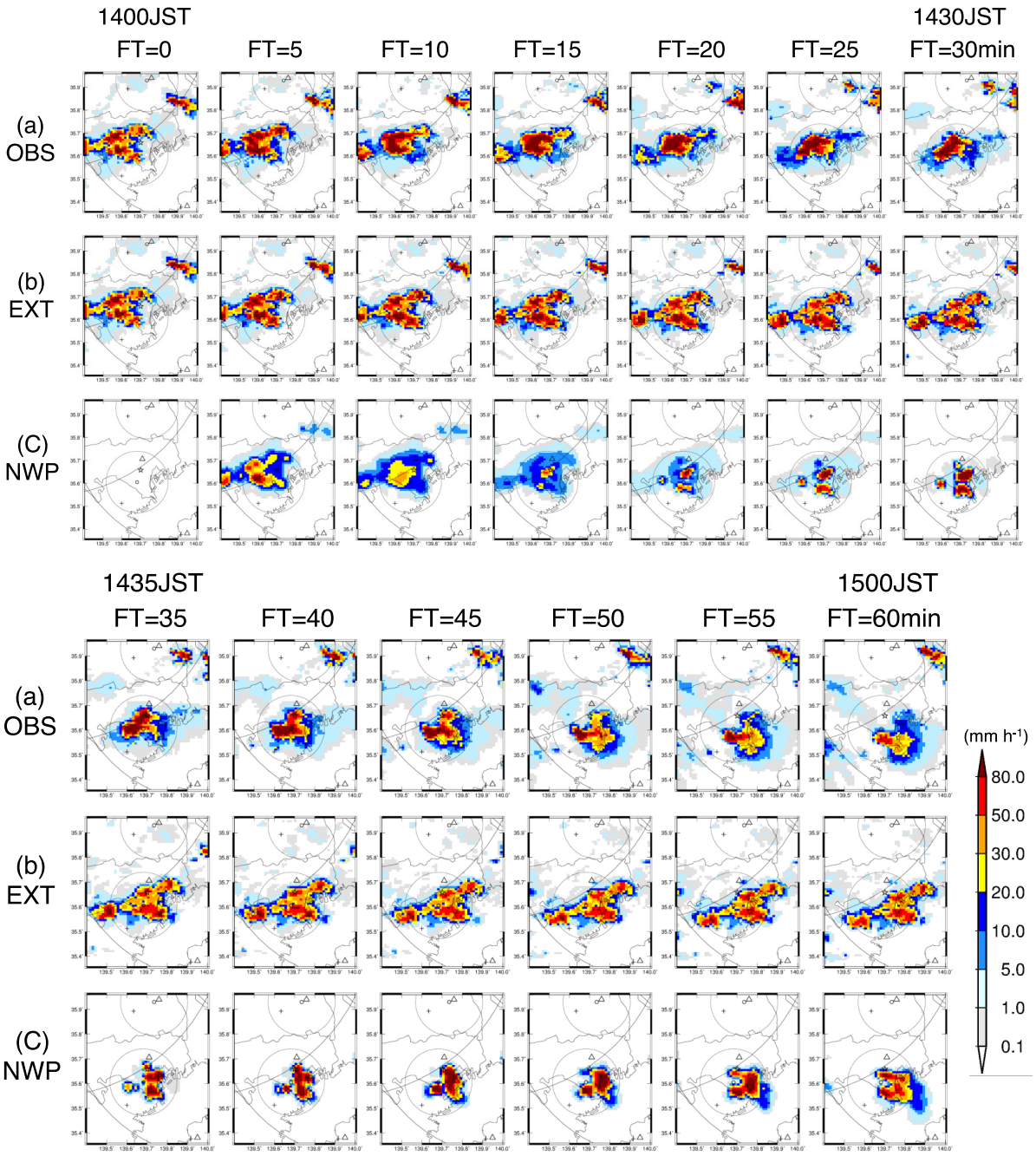

Fig. 2. Time series of rainfall rate (mm h^{-1}) of (a) OBS, (b) EXT, and (c) NWP from 14:00-15:00 JST on 24 July 2015. The area plotted in this figure corresponds to the verification domain in **Fig. 1**.

the heavy rainfall event was meso-γ-scale. Thus, this event satisfied the conditions of a MγExHR event ($P1h_{max} \geq 50$ mm and $L_h \leq 10$ km) used in [7]. In this study, the predictions of the EXT and NWP model (CReSS-0.7km) were started at 14:00 JST, or 30 min before the onset of the extremely heavy rainfall of ≥80 mm h^{-1} was analyzed at the Shibuya railway station.

5.2. Time Evolution of Rainfall Rate

The time series of observed (OBS), EXT, and NWP rainfall rates from 14:00–15:00 JST on 24 July 2015 are shown in **Fig. 2**. In the NWP experiment, all available observational data were assimilated with VR, Z, and PWV. In the OBS time series (**Fig. 2a**), an area of heavy rainfall of ≥20 mm h^{-1} was observed to the west of Shibuya station at FT = 0 min. Until FT = 35 min, the area of heavy rainfall moved east-southeastward, with its peak value nearly preserved but with the areal extent of the rainfall ≥20 mm h^{-1} decreasing. After FT=40 min, the direction of movement changed to the south-southeast, but the area of rainfall ≥20 mm h^{-1} changed little, although the strength of the storm seemed to weaken because the area of rainfall ≥50 mm h^{-1} decreased. For the EXT time series (**Fig. 2b**), the area of heavy rainfall ≥20 mm h^{-1}

moved to the east-southeast with its areal extent almost preserved until FT = 60 min. The locations of the EXT and OBS areas of heavy rainfall were similar until FT = 60 min; however, the areal extent of rainfall $\geq$20 mm h^{-1} of the EXT was greater than that of the OBS.

In the time series of rainfall rate predicted by the NWP model (**Fig. 2c**), there was no rainfall at FT = 0 min, unlike in the case of both OBS and EXT. This is because assimilation of Z introduces a 3D precipitation distribution above the surface at FT = 0 min. The rainfall rate of CReSS was calculated strictly using the vertical flux of the sum of the precipitation species at the lowest level of CReSS (z = 50 m). Since (1) no precipitation species were predicted by the 1km-CReSS at the level at 14:00 JST (FT = 0) and (2) no precipitation species were introduced by the assimilation of Z at the level at FT = 0, the rainfall rate of the NWP was zero at FT = 0. The precipitation introduced above the surface fell to the surface, resulting in an area of heavy rainfall of $\geq$20 mm h^{-1} and locally an extremely heavy rainfall of $\geq$50 mm h^{-1} at FT = 5 min. At FT = 10 min, the area of extremely heavy rainfall of $\geq$50 mm h^{-1} disappeared, which indicates weakening of the surface rainfall. At FT = 15 min, the area of rainfall of $\geq$20 mm h^{-1} decreased further; however, an area of extremely heavy rainfall of $\geq$50 mm h^{-1} reappeared. The areal extents of the rainfall of $\geq$50 and $\geq$20 mm h^{-1} at FT = 15 min developed until FT = 40 min. After 40 min, the area of rainfall of $\geq$20 mm h^{-1} did not change much. The behavior of the area of heavy rainfall predicted by the NWP model can be categorized into three stages: (1) the decay stage (FT = 5–15 min), (2) redevelopment stage (FT = 15–40 min), and (3) mature stage (FT = 40–60 min). The decay and redevelopment stages of the area of heavy rainfall predicted by the NWP model during FT=5 to 40 min were not observed (**Fig. 2a**), indicating that this process is most likely an artifact due to the introduction of 3D precipitation distribution above the surface and modification of moisture through the assimilation of Z. However, the areas of heavy rainfall predicted by the NWP model were similar to those of the OBS after the redevelopment stage, or after FT = 40 min.

5.3. Quantitative Verification Using FSS

To compare the forecast accuracies of the EXT and the NWP models quantitatively, the FSS for the rainfall threshold of 20 mm h^{-1} for L=11 km as a function of forecast time is shown in **Fig. 3(a)**. The accuracy of the EXT decreased until FT=30 min; thereafter, it remained nearly constant from FT=30 to 50 min, and it decreased after 50 min. The accuracy of the NWP model decreased rapidly until FT=15 min; thereafter, it increased from FT=15 to 50 min, and it decreased again after FT=50 min. The time evolution of the forecast accuracy of the NWP model until FT=50 min is reflected in the decay and redevelopment of the area of heavy rainfall area due to the assimilation of Z, which will be described in section 6 in more detail. The decrease in forecast accuracy after FT=50 min for both the EXT and the NWP models was attributable mainly to the increase in displacement error of the heavy rainfall area due to the southward movement of the observed area of heavy rainfall (**Fig. 2a**). Note, the accuracy of the EXT in this case, FSS (L=11 km) = 0.73 at FT=30 min, was much higher than the average accuracy of the EXT for the 23 MγExHR events, FSS(L=11km) = 0.50 at FT=30 min (see Fig. 9b in [7]). This is probably because the observed area of heavy rainfall propagated somewhat steadily and did not change dramatically in the analyzed period (14:00–15:00 JST) in this study. In such a situation, an EXT usually provides a highly accurate forecast.

The forecast accuracy of the NWP model was lower than that of the EXT before FT=35 min (**Fig. 3a**); however, the accuracy of the NWP model outperformed the EXT after FT=40 min. As an example, we compared the rainfall rate distribution at FT=50 min, when the FSS showed that the NWP model largely outperformed the EXT. The EXT (**Fig. 2b**) overpredicted the area of rainfall of $\geq$20 mm h^{-1}, whereas the NWP model (**Fig. 2c**) predicted the area of heavy rainfall more correctly.

The results shown above were achieved based on the FSS for a value of L=11 km. However, here, we show the forecast accuracy for a more severe situation involving displacement error of heavy rainfall areas by examining the FSS for smaller values of L (**Fig. 3b** and **3c**). The smaller the value of L was, the smaller the FSS values of EXT and NWP were, but the tendency of the time evolution of the FSSs was similar to that for L=11 km. Even for grid-scale verification (for L=1 km; **Fig. 3c**), the FSS of the NWP exceeded that of the EXT after FT=45 min. This result suggests that an NWP with storm-scale data assimilation has the potential to outperform an EXT in the prediction of the areal extent of heavy rainfall of $\geq$20 mm h^{-1} for an MγExHR event over a very short time range of $\leq$1 h, e.g., after 45 min; L=1 km.

6. Discussion

In this section, we discuss why the NWP predicted the heavy rainfall area near Shibuya station over the very short time range of $\leq$1 h more correctly than did the EXT, as shown in the previous section. To discuss the factors, we performed three additional sensitivity experiments with different assimilation methods of radar reflectivity. The control experiment (CNTL) was the same experiment shown in the previous section, where both precipitation and moisture were modified in the reflectivity assimilation. In the first experiment (NOPrep), the 3D distribution of precipitation was not introduced in the reflectivity assimilation. In the second experiment (NOQV), no moisture adjustment was made, i.e., the 3D distribution of water vapor was not modified, in the reflectivity assimilation. In the third experiment (NORef), there was no reflectivity assimilation, i.e., both precipitation and moisture were left unmodified.

Time series of the rainfall rates of these experiments from 14:00–15:00 JST are shown in **Fig. 4**. In the NORef

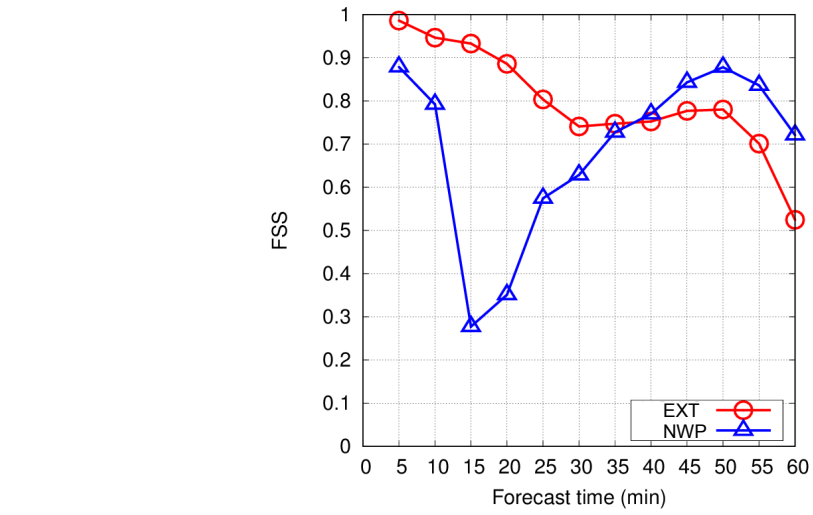

(a) L=11 km

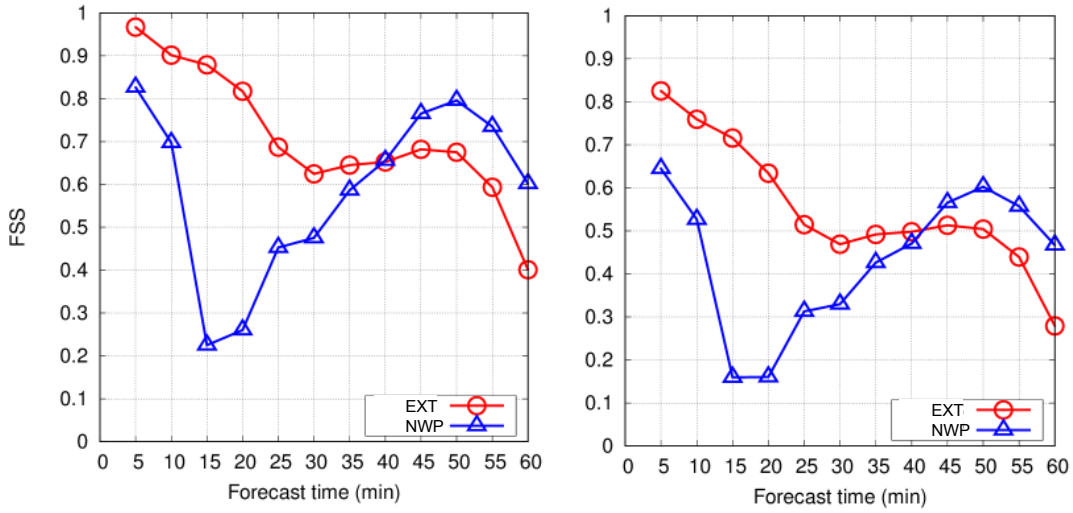

(b) L=5 km (c) L=1 km

Fig. 3. FSS for spatial scales of displacement error L of (a) 11, (b) 5, and (c) 1 km for the EXT and NWP(CNTL) forecasts commenced at 14:00 JST.

experiment (**Fig. 4e**), the time evolution of rainfall was quite different from that of OBS and CNTL. No rain occurred before FT=25 min, and only a very localized rainfall area appeared after FT=35 min. A comparison of the CNTL and NORef experiments indicates that the assimilation of Z was essential to the prediction of MγExHR after 35 min in this study. In the NOQV experiment (**Fig. 4d**), heavy rainfall area appeared at FT=5min because of the introduction of the 3D distribution of precipitation above the ground, and the heavy rainfall area decayed until FT=15 min. This time evolution of the decay stage was similar to that of CNTL. However, the redevelopment of the heavy rainfall area near Shibuya station simulated in CNTL was not simulated in NOQV, and only a very localized rainfall area appeared to the south of Shibuya station after FT=25 min. In the NOPrep experiment (**Fig. 4c**), no rain occurred until FT=25 min because precipitation was not introduced by the assimilation of Z. After 25 min, a heavy rainfall area appeared, and the time evolution of this heavy rainfall area was similar to that of the CNTL.

A comparison of these four experiments indicates that the redevelopment of the heavy precipitation area in the CNTL experiment after 15 min was due to the moisture adjustment in the assimilation of Z and that this moisture adjustment was essential for the forecast of the heavy rainfall area after FT=25 min.

It is also indicated that the introduction of the 3D distribution of precipitation above the surface helped to forecast the initial time evolution of the heavy precipitation area, but it did not help after FT=25 min because of the decay of the heavy precipitation area. The cause of the decay of the heavy precipitation was probably unbalanced vertical velocity and temperature fields in the initial conditions that could not sustain and correctly evolve the 3D distribution of the precipitation field. For 3DVAR, it is a challenging task to introduce such balanced fields as initial conditions. We are tackling the problem using a thermodynamic retrieval method [39–41], and the results will be reported as future studies.

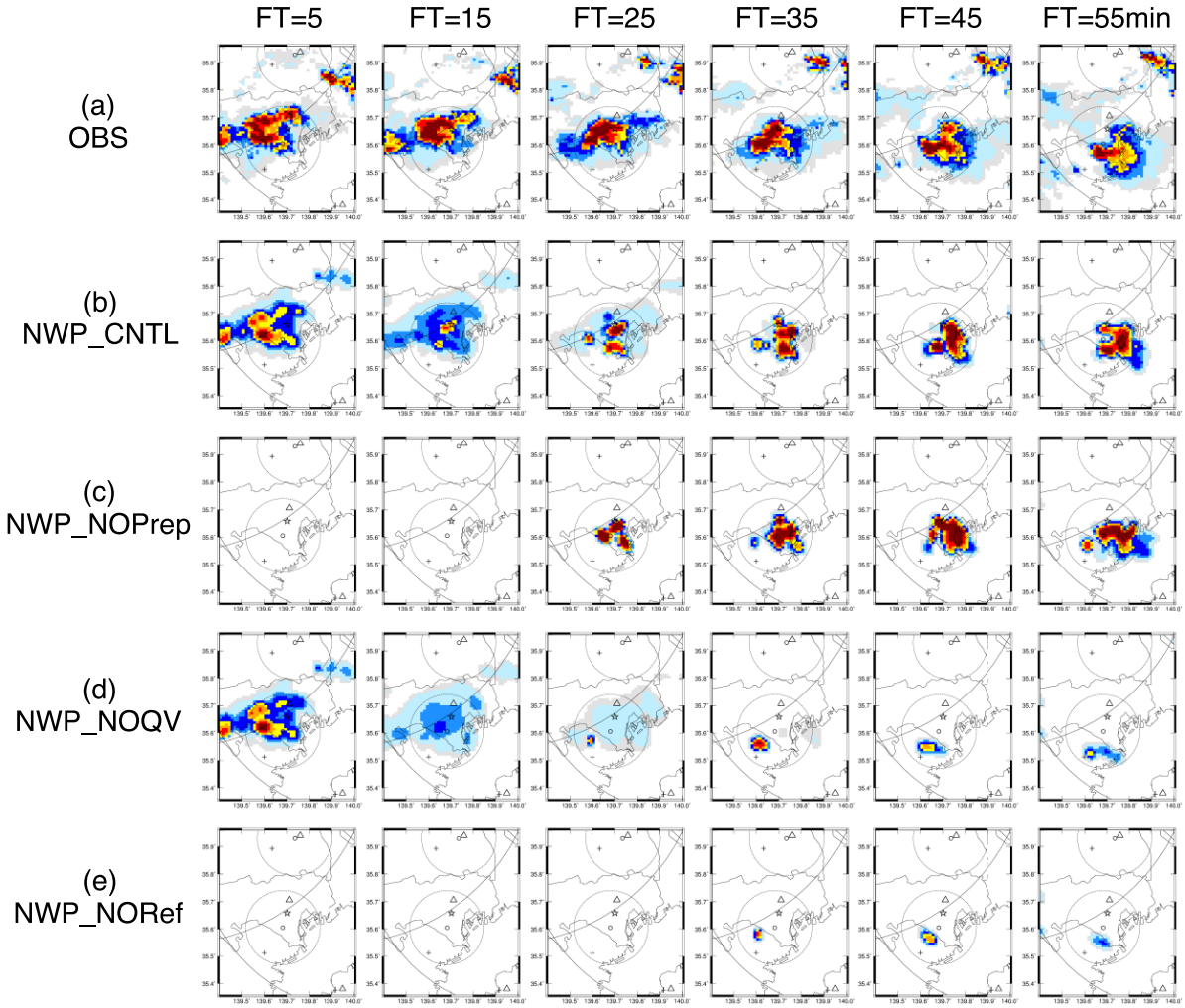

Fig. 4. Time series of rainfall rates of (a) OBS and (b-f) NWP experiments examining the assimilation impact of reflectivity from 14:05-14:55 JST. (a) and (b) are the same as (a) and (c) in **Fig. 2**, respectively.

7. Summary and Future Work

The occurrence of an MγExHR can cause urban flash flooding with accompanying damage and potential loss of life. Thus, it is vital that a method for forecasting an MγExHR be developed and verified. Some studies of MγExHRs with very short time scales ($\leq$1 h) have used NWP models with storm-scale data assimilation; however, they did not compare the accuracies of the NWP forecast and the EXT. In this study, the forecast accuracy of an NWP model over a very short time range ($\leq$1 h), for an MγExHR event that caused flooding at the Shibuya railway station in Japan on 24 July 2015, was compared with that of an EXT. For the EXT, HRPNs provided by the JMA were used. For the NWP model, a high-resolution (0.7 km) CReSS was used with a 3DVAR data assimilation system called CReSS-3DVAR. For the CReSS-3DVAR, unique storm-scale observational data obtained from dense networks of radars, lidars, and MWRs, developed in the Tokyo metropolitan area by NIED, were assimilated. The forecast accuracy of the area of heavy rainfall ($\geq$20 mm h^{-1}) as a function of FT was investigated for the NWP model and EXT predictions using FSS for various spatial scales of L. These predictions were started $\sim$30 min before the time of onset of the extremely heavy rainfall at the railway Shibuya station.

The FSS for L=1 km, i.e., grid-scale verification, showed that the accuracy of the NWP model was lower than that of EXT before FT=40 min. However, the NWP model outperformed the accuracy of the EXT from FT=45 to 60 min. This result suggests that an NWP model with storm-scale data assimilation has the potential to outperform an EXT in the prediction of the area of heavy rainfall of $\geq$20 mm h^{-1} for an MγExHR event over the very short time range of $\leq$1 h, e.g., after 45 min. It also suggests that it should be possible to provide a seamless high-accuracy forecast for an area of heavy rainfall of $\geq$20 mm h^{-1} for an MγExHR event over very short time range ($\leq$1 h) by blending the EXT and the NWP outputs. The possibility of providing a seamless forecast by using a blending method is supported by the similar location of the heavy rainfall area forecast in the EXT and by the NWP at $\sim$45 min in this study.

As the results in this study were obtained from a sin-

gle case, other MγExHR events should be investigated. In particular, the period evaluated in this study was a time during which the area of heavy rainfall propagated somewhat steadily and did not change dramatically. In such a situation, an EXT usually provides a highly accurate forecast. Furthermore, an NWP model has the ability to predict the generation of convective clouds, whereas an EXT does not. Thus, it is necessary to examine the forecast accuracies of NWP models and EXTs for when convective clouds are generated within the area of dense observational networks. We are currently examining just such an MγExHR event.

Acknowledgements

The authors thank the Ministry of Land, Infrastructure, Transport, and Tourism (MLIT) for providing data from the MLIT's X-band MP radars via DIAS. The DIAS data set is archived and provided under the framework of the Data Integration and Analysis System (DIAS) through the National Key Technology, Marine Earth Observation Exploration System. This work was supported by the Council for Science, Technology and Innovation (CSTI), Cross-ministerial Strategic Innovation Promotion Program (SIP), and "Enhancement of societal resiliency against natural disasters" (Funding agency: JST). Two anonymous reviewers provided very useful comments. The dense observation network in the Tokyo metropolitan area was operated by the members of NIED (Takeshi Maesaka, Shin-ichi Suzuki, Yukari Shusse, Namiko Sakurai, Kaori Kieda, Yasushi Uji, Ryohei Misumi, and the authors).

References:

[1] A. Kato and M. Maki, "Localized heavy rainfall near Zoshigaya, Tokyo, Japan on 5 August 2008 observed by X-band polarimetric radar – Preliminary analysis –," Sola, Vol.5, pp. 89-92, 2009.

[2] D. S. Kim, M. Maki, S. Shimizu, and D. I. Lee, "X-Band dual-polarization radar observations of precipitation core development and structure in a multi-cellular storm over Zoshigaya, Japan, on August 5, 2008," J. Meteor. Soc. Japan, Vol.90, pp. 701-719, 2012.

[3] C. Pierce, A. Seed, S. Ballard, D. Simonin, and Z. Li, "Nowcasting. Doppler radar observations – weather radar, wind profiler," in ionospheric radar, and other advanced applications, Bech J and Chau JL (Eds.), Rijeka: InTech, pp. 97-142, 2012.

[4] S. P. C., R. Misumi, T. Nakatani, K. Iwanami, M. Maki, A. W. Seed, and K. Hirano, "Comparison of rainfall nowcasting derived from the STEPS model and JMA precipitation nowcasts," Hydrol. Res. Lett., Vol.9, pp. 54-60, 2015.

[5] J. Sun, M. Xue, J. W. Wilson, I. Zawadzki, S. P. Ballard, J. Onvlee-Hooimeyer, P. Joe, D. M. Barker, P. W. Li, B. Golding, M. Xu, and J. Pinto, "Use of NWP for nowcasting convective precipitation: Recent progress and challenges," Bull. Am. Meteorol. Soc., Vol.95, pp. 409-426, 2014.

[6] Y. Hwang, A. J. Clark, V. Lakshmanan, and S. E. Koch, "Improved nowcasts by blending extrapolation and model forecasts," Wea. Forecasting, Vol.30, pp. 1201-1217, 2015.

[7] R. Kato, S. Shimizu, K. Shimose, T. Maesaka, K. Iwanami, and H. Nakagaki, "Predictability of meso-γ-scale, localized, extreme, heavy rainfall during the warm season in Japan using high-resolution precipitation nowcasts," Q. J. R. Meteorol. Soc., Vol.143, pp. 1406-1420, 2017.

[8] S. Kigawa, "Techniques of precipitation analysis and prediction for high-resolution precipitation nowcasts," p. 15, 2014, available online at http://www.jma.go.jp/jma/en/Activities/Techniques_of_Precipitation_Analysis_and_Prediction_developed_for_HRPNs.pdf [accessed March 29, 2017]

[9] S. Kigawa, "Techniques of precipitation analysis and prediction for high-resolution precipitation nowcasts," Weather service bulletin, Vol.81, p. 22, 2014 (in Japanese), available online at http://www.jma.go.jp/jma/kishou/books/sokkou/81/vol81p055.pdf [accessed March 29, 2017]

[10] N. M. Roberts and H. W. Lean, "Scale-selective verification of rainfall accumulations from high-resolution forecasts of convective events," Mon. Wea. Rev., Vol.136, pp. 78-97, 2008.

[11] K. Nagata, "Quantitative precipitation estimation and quantitative precipitation forecasting by the Japan meteorological agency," RSMC Tokyo Typhoon Center Technical Review, Vol.13, pp. 37-50, 2011, available online at http://www.jma.go.jp/jma/jma-eng/jma-center/rsmc-hp-pub-eg/techrev/text13-2.pdf [accessed March 29, 2017]

[12] T. Kawabata, H. Iwai, H. Seko, Y. Shoji, K. Saito, S. Ishii, and K. Mizutani, "Cloud-resolving 4D-var assimilation of Doppler wind lidar data on a meso-gamma-scale convective system," Mon. Wea. Rev., Vol.142, pp. 4484-4498, 2014.

[13] T. Miyoshi, M. Kunii, J. Ruiz, G. Lien, S. Satoh, T. Ushio, K. Bessho, H. Seko, H. Tomita, and Y. Ishikawa, ""Big data assimilation" revolutionizing severe weather prediction," Bull. Amer. Meteor. Soc., Vol.97, pp. 1347-1354, 2016.

[14] K. Tsuboki and A. Sakakibara, "Large-scale parallel computing of cloud resolving storm simulator," in Lecture Notes in Computer Science, High Performance Computing, ISHPC 2002, Vol.2327, H. P. Zima, K. Joe, M. Sato, Y. Seo, and M. Shimasaki (Eds.), Berlin: Springer, pp. 243-259, 2002.

[15] K. Tsuboki and A. Sakakibara, "Numerical prediction of high-impact weather systems," The text book for Seventeenth IHP training course in 2007, HyARC, Nagoya University, Japan, and UNESCO, p. 281, 2007.

[16] T. Maesaka, M. Maki, K. Iwanami, S. Tsuchiya, K. Kieda, and A. Hoshi, "Operational rainfall estimation by X-band MP radar network in MLIT, Japan," Preprints, 35th Conf. on Radar Meteor., Pittsburgh, PA, Amer. Meteor. Soc., 29 Sep. 2011.

[17] F. Solheim, J. R. Godwin, E. R. Westwater, Y. Han, S. J. Keihm, K. Marsh, and R. Ware, "Radiometric profiling of temperature, water vapor and cloud liquid water using various inversion methods," Radio Sci., Vol.33, pp. 393-404, 1998.

[18] M. Murakami, T. L. Clark, and W. D. Hall, "Numerical simulation of convective snow clouds over the Sea of Japan; two-dimensional simulations of mixed layer development and convective snow cloud formation," J. Meteor. Soc. Japan, Vol.72, pp. 43-62, 1994.

[19] J. W. Deardorff, "Three-dimensional numerical study of the height and mean structure of a heated planetary boundary layer," Boundary-Layer Meteor., Vol.7, pp. 81-106, 1974.

[20] J. W. Deardorff, "Stratocumulus-capped mixed layers derived from a three-dimensional model," Boundary-Layer Meteor., Vol.18, pp. 495-527, 1980.

[21] J. F. Louis, M. Tiedtke, and J. F. Geleyn, "A short history of the operational PBL parameterization at ECMWF," Preprints, Workshop on Planetary Boundary Layer Parameterization, Shinfield Park, Reading, ECMWF, 25-27 Nov. 1981.

[22] J. Kondo, "Air-sea bulk transfer coefficients in diabatic conditions," Boundary-Layer Meteor., Vol.9, pp. 91-112, 1975.

[23] A. Segami, K. Kurihara, H. Nakamura, M. Ueno, I. Takano, and Y. Tatsumi, "Operational mesoscale weather prediction with Japan Spectral Model," J. Meteor. Soc. Japan, Vol.67, pp. 907-924, 1989.

[24] D. M. Barker, W. Huang, Y.-R. Guo, and A. Bourgeois, "A three-dimensional variational (3DVAR) data assimilations system for use with MM5," NCAR Tech. Note. NCAR/TN-453 + STR, NCAR, p. 68, 2003.

[25] D. M. Barker, W. Huang, Y.-R. Guo, A. J. Bourgeois, and Q. N. Xiao, "A three-dimensional variational data assimilation system for MM5: implementation and initial results," Mon. Wea. Rev., Vol.132, pp. 897-914, 2004.

[26] D. P. Dee and A. M. Da Silva, "The Choice of Variable for Atmospheric Moisture Analysis," Mon. Wea. Rev., Vol.131, pp. 155-171, 2003.

[27] T. Kawabata, H. Seko, K. Saito, T. Kuroda, K. Tamiya, T. Tsuyuki, Y. Honda, and Y. Wakazuki, "An assimilation and forecasting experiment of the Nerima heavy rainfall with a cloud-resolving nonhydrostatic 4-dimensional variational data assimilation system," J. Meteor. Soc. Japan, Vol.85, pp. 255-276, 2007.

[28] J. Gao et al., "A realtime weather-adaptive 3DVAR analysis system for severe weather detections and warnings with automatic storm positioning capability," Wea. Forecasting, Vol.28, pp. 727-745.

[29] P. Courtier and J. N. Thépaut, and A. Hollingsworth, "A strategy for operational implementation of 4D-Var, using an incremental approach," Quart. J. Roy. Meteor. Soc., Vol.120, pp. 1367-1388, 1994.

[30] P. Courtier, "Dual formulation of four-dimensional variational assimilation," Quart. J. Roy. Meteor. Soc., Vol.123, pp. 2449-2461, 1997.

[31] X. Zou, I. M. Navon, M. Berger, K. H. Phua, T. Schlick, and F. X. Le Dimet, "Numerical experience with limited-memory quasi-Newton and truncated Newton methods," SIAM J. on Optimization, Vol.3, pp. 582-608, 1993.

[32] A. J. Koscielny, R. J. Doviak, and R. Rabin, "Statistical considerations in the estimation of divergence from single-Doppler radar and application of prestorm boundary-layer observations," J. Appl. Meteor., Vol.21, pp. 197-210, 1982.
[33] R. R. Rogers, "An extension of the ZR relation for Doppler radar," Preprints, 11th Conf. on Radar Meteor., Boulder, CO, Amer. Meteor. Soc., pp. 158-161, 1964.
[34] P. W. Baker and M. C. Hodson, "Effect of deviations from the Marshall-Palmer drop size distribution on the calculation of vertical air velocity by Rogers's method," Vol.24, pp. 495-498, 1985.
[35] A. Lorenc, "Iterative analysis using covariance functions and filters," Quart. J. Roy. Meteor. Soc., Vol.118, pp. 569-591, 1992.
[36] C. M. Hayden and R. J. Purser, "Recursive filter objective analysis of meteorological fields: application to NESDIS operational processing," J. Appl. Meteor., Vol.34, pp. 3-15, 1995.
[37] R. J. Purser, W.-S. Wu, D. F. Parrish, and N. M. Roberts, "Numerical aspects of the application of recursive filter to variational statistical analysis. Part I: spatially homogeneous and isotropic Gaussian covariance," Mon. Wea. Rev., Vol.131, pp. 1524-1535, 2003.
[38] D. F. Parrish and J. C. Derber, "The National Meteorological Center's spectral statistical-interpolation analysis system," Mon. Wea. Rev., Vol.120, pp. 1747-1763, 1992.
[39] Y. Lin, P. S. Ray, and K. W. Johnson, "Initialization of a modeled convective storm using Doppler radar-derived fields," Mon. Wea. Rev., Vol.121, pp. 2757-2775, 1993.
[40] S. S. Weygandt, A. Shapiro, and K. K. Droegemeier, "Retrieval of model initial fields from single-Doppler observations of a supercell thunderstorm. Part II: Thermodynamic retrieval and numerical prediction," Mon. Wea. Rev., Vol.130, pp. 454-476, 2002.
[41] Y. Liou, J. Chiou, W. Chen, and H. Yu, "Improving the Model Convective Storm Quantitative Precipitation Nowcasting by Assimilating State Variables Retrieved from Multiple-Doppler Radar Observations," Mon. Wea. Rev., Vol.142, pp. 4017-4035, 2014.
[42] M. Hu, M. Xue, and K. Brewster, "3DVAR and cloud analysis with WSR-88D level-II data for the prediction of the Fort Worth, Texas, tornadic thunderstorms. Part I: Cloud analysis and its impact," Mon. Wea. Rev., Vol.134, pp. 675-698, 2006.
[43] O. Caumont, V. Ducrocq, É. Wattrelot, G. Jaubert, and S. Pradier-Vabre, "1D+3DVar assimilation of radar reflectivity data: A proof of concept," Tellus, Vol.62A, pp. 173-187, 2010.
[44] E. Wattrelot, O. Caumont, J. F. Mahfouf, "Operational implementation of the 1D+3D-Var assimilation method of radar reflectivity data in the AROME model," Mon. Weather Rev., Vol 142, pp. 1852-1873, 2014.
[45] J. Gao and D. J. Stensrud, "Assimilation of reflectivity data in a convective-scale, cycled 3DVAR framework with hydrometeor classification," J. Atmos. Sci., Vol.69, pp. 1054-1065, 2012.
[46] P. L. Jr. Smith, C. G. Myers, and H. D. Orville, "Radar reflectivity factor calculations in numerical cloud models using bulk parameterization of precipitation processes," J. Appl. Meteor., Vol.14, pp. 1156-1165, 1975.
[47] D. Hauser and P. Ameyanc, "Retrieval of cloud water and water vapor contents from Doppler radar data in a tropical squall line: Application to the case of a tropical squall line," J. Atmos. Sci., Vol.43, pp. 823-838, 1986.
[48] K. Saito, T. Fujita, Y. Yamada, J. Ishida, Y. Kumagai, K. Aranami, S. Ohmori, R. Nagasawa, S. Kumagai, C. Muroi, T. Kato, H. Eito, and Y. Yamazaki, "The operational JMA nonhydrostatic mesoscale model," Mon. Wea. Rev., Vol.134, pp. 1266-1298, 2006.

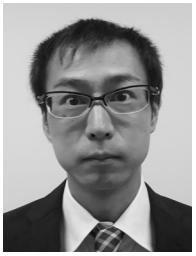

Name:
Ryohei Kato

Affiliation:
Associate Research Fellow, Storm, Flood and Landslide Research Division, National Research Institute For Earth Science and Disaster Resilience (NIED)

Address:
3-1 Tennodai, Tsukuba, Ibaraki 305-0006, Japan

Brief Career:
2012 Visiting Scientist, Meteorological Research Institute, Japan Meteorological Agency
2015 Associate Research Fellow, National Research Institute For Earth Science and Disaster Resilience

Selected Publications:
• R. Kato, K. Kusunoki, E. Sato, W. Mashiko, H. Y. Inoue, C. Fujiwara, K. Arai, M. Nishihashi, S. Saito, S. Hayashi, and H. Suzuki, "Analysis of the horizontal two-dimensional near-surface structure of a winter tornadic vortex using high-resolution in situ wind and pressure measurements," J. Geophys. Res. Atmos., Vol.120, pp. 5879-5894, 2015.
• R. Kato, S. Shimizu, K. Shimose, T. Maesaka, K. Iwanami, and H. Nakagaki, "Predictability of meso-γ-scale, localized, extreme, heavy rainfall during the warm season in Japan using high-resolution precipitation nowcasts," Q. J. R. Meteorol. Soc., Vol.143, pp. 1406-1420, 2017.

Academic Societies & Scientific Organizations:
• Meteorological Society of Japan (MSJ)
• American Meteorological Society (AMS)

Name:
Shingo Shimizu

Affiliation:
Senior Researcher, Storm, Flood and Landslide Research Division, National Research Institute For Earth Science and Disaster Resilience (NIED)

Address:
3-1 Tennodai, Tsukuba, Ibaraki 305-0006, Japan

Brief Career:
2006 Associate Research Fellow, NIED
2008 Researcher with Tenure, NIED
2012 Senior Researcher, NIED

Selected Publications:
• "Algorithm for the identification and tracking convective cells based on constant and adaptive threshold methods using a new cell-merging and -splitting scheme," J. Meteor. Soc. Japan, Vol.90, pp. 868-889, 2012.
• "Structure and formation mechanism of a 24 May 2000 supercell-like storm developing in a moist environment over Kanto Plain," Japan. Mon. Wea. Rev., Vol.136, pp. 2389-2407, 2007.
• S. Shimizu, "Multiple Doppler radar analysis for retrieving the three-dimensional wind field within thunderstorm," InTech Press, Chapter 9 in "Doppler radar observations," p. 482, 2012.

Academic Societies & Scientific Organizations:
• Meteorological Society of Japan (MSJ)

Name:
Ken-ichi Shimose

Affiliation:
Associate Research Fellow, Storm, Flood and Landslide Research Division, National Research Institute For Earth Science and Disaster Resilience (NIED)

Address:
3-1 Tennodai, Tsukuba, Ibaraki 305-0006, Japan

Brief Career:
2009-2011 Visiting Scientist, Meteorological Research Institute, Japan Meteorological Agency
2011-2013 Postdoctoral Researcher, National Institute of Advanced Industrial Science and Technology
2014- Associate Research Fellow, National Research Institute For Earth Science and Disaster Resilience

Selected Publications:
• K. Shimose, M. Xue, R. D. Palmer, J. Gao, B. L. Cheong, and D. Bodine, "Two-dimensional Variational Analysis of Near-Surface Moisture from Simulated Radar Refractivity-related Phase Change Observations," Advances in Atmospheric Sciences, Vol.30, pp. 291-305, 2013.
• K. Shimose, S. Shimizu, T. Maesaka, R. Kato, K. Kieda, and K. Iwanami, "Impact of Observation Operators on Low-Level Wind Speed Retrieved by Variational Multiple-Doppler Analysis," SOLA, Vol.12, pp. 215-219, 2016.

Academic Societies & Scientific Organizations:
• Meteorological Society of Japan (MSJ)
• American Meteorological Society (AMS)
• Institute of Electrical Engineers of Japan (IEEJ)

Name:
Koyuru Iwanami

Affiliation:
Principal Chief Researcher, Storm, Flood and Landslide Research Division, National Research Institute for Earth Science and Disaster Resilience (NIED)

Address:
3-1 Tennodai, Tsukuba, Ibaraki 305-0006, Japan

Brief Career:
1991 Joined National Research Institute for Earth Science and Disaster Prevention (NIED)
2002-2003 Visiting Scientist, CETP/CNRS, France
2013-2016 Director, Storm, Flood and Landslide Research Unit, NIED

Selected Publications:
• S. G. Park, M. Maki, K. Iwanami, V. N. Bringi, and V. Chandrasekar, "Correction of Radar Reflectivity and Differential Reflectivity for Rain Attenuation at X-band. Part II: Evaluation and Application," Journal of Atmospheric and Oceanic Technology, Vol.22, pp. 1633-1655, 2005.

Academic Societies & Scientific Organizations:
• American Meteorological Society (AMS)
• Meteorological Society of Japan (MSJ)
• Japanese Society of Snow and Ice (JSSI)
• Japan Geoscience Union (JpGU)